The studies of a new photon detector for $K_L \to \pi^0 \nu \bar{\nu}$ experiment at J-PARC

Yoshiteru Shibata
High Energy Physics Group
Department of Physics at Osaka University

February 10, 2004

Abstract

We studied a new photon detector which can measure the direction of the photon. For photons with the energies between 1.5 and 2.7 GeV, the angular resolution was $\frac{154\pm30_{(stat.)}\pm7_{(sys)}}{\sqrt{E}}$ (mrad), where E is the photon energy in GeV. At the center of the 3×3 shashlik tower, the position resolution was $(\frac{0.45\pm0.08}{\sqrt{E}} + (0.57 \pm 0.06))$ cm, and the energy resolution was $(\frac{11.40\pm0.06}{\sqrt{E}} \oplus (0.0 \pm 0.7))$ %, where E is the photon energy in GeV.

Acknowledgements

It is my pleasure to be able to thank the many people who have helped make the last for two years so enjoyable and rewarding. First and foremost, I would like to thank Prof. Taku Yamanaka, my supervisor, for guiding my studies with precision, enthusiasm, good humor and endless patience. He has been an enormous source of encouragement and inspiration, and is largely responsible for teaching me how to do research. Heartfelt thanks go to T.Hara, K.Sumisawa and M.Yamaga, whose clear and precise comments and explanations over the years have been very much appreciated.

Special thanks must go to T.Nakano, Y.Sugaya, A.Shimizu, and LEPS collaborator. In particularly, I would like to thank Y.Sugaya. He gave me many valuable advices about DAQ system and experiment techniques. I would like to thank H.Watanabe and E391a collaborators.

Special thanks go to Hakuyo Engineering Co. (Higashiosaka-shi, Osaka) who help us constructing the detector.

My special thanks go to K.Sakashita, S.Komatsu, Y.Shimada, and N.Nishi, who gave me invaluable advice as members of this experiment. I also owe a lot to the members of the Yamanaka Taku Group at Osaka University for the good companionship and encouragement, T.Houjo, K.Kotera, H.Miyake, K.Hara, Y.Ikemoto, and E.Tanaka. I would like to thank go to N.Sugimoto who help and support for my research life.

Last, I would like to thank my parents for far more than I could possibly describe here.

Contents

1 Introduction **9**
- 1.1 CP violation . . . 9
- 1.2 CKM matrix . . . 10
- 1.3 Decay of $K_L \to \pi^0\nu\bar{\nu}$ . . . 11
- 1.4 Background for $K_L \to \pi^0\nu\bar{\nu}$ experiment . . . 11
- 1.5 Motivation and Overview . . . 13

2 Study of basic parameters of a new photon detector **14**
- 2.1 The concept of a new detector . . . 14
- 2.2 Geant Simulation . . . 14
  - 2.2.1 Thickness of lead and scintillator . . . 16
  - 2.2.2 Optimum number of layers for each block . . . 16
- 2.3 Fiber response test for GEANT simulation . . . 18

3 Shashlik calorimeter **20**
- 3.1 shashlik calorimeter . . . 20
  - 3.1.1 Lead/Scintillator . . . 20
  - 3.1.2 Wave length shifting fiber . . . 21
  - 3.1.3 64ch Multi Anode PMT . . . 23
  - 3.1.4 Fiber blackout . . . 25

4 The outline of the experiment at SPring8 **27**
- 4.1 Beam . . . 27
- 4.2 Detector summary . . . 27
  - 4.2.1 Collimater . . . 27
  - 4.2.2 Veto counter . . . 28
- 4.3 Experiment . . . 28
- 4.4 Trigger . . . 30
- 4.5 Data acquisition . . . 30
- 4.6 Run Summary . . . 30

5 Detector calibration **33**
- 5.1 The flow of detector calibration . . . 33
- 5.2 Event selection . . . 33

5.3 Gain calibration of fibers in the shower profile counter 33
5.4 Comparison between shower profile counter and Geant Simulation 34
5.5 Gain calibration for SHASHLIK with 64ch MAPMT 35

6 Data Analysis **40**
6.1 Position resolution 40
6.2 Angle resolution 43
6.2.1 Distances between the blocks 43
6.2.2 Angle reconstruction 43
6.3 Energy resolution 47

7 Systematic error on the angular resolution **49**
7.1 Systematic error due to gain calibration 49
7.2 Systematic error due to the shower profile generated by Geant . 49
7.3 Systematic error summary 53

8 Geant simulation **54**

9 Discussions **56**
9.1 The difference between the data and MC 56
9.2 Analytic method 56
9.3 Improvements of the performances 56

10 Conclusion **58**

List of Figures

1.1 Feynman diagram for the decay $K_L \to \pi^0 \nu\bar{\nu}$ 12

2.1 The strategy to measure the direction of the photon 15
2.2 A design of a new photon detector 15
2.3 Energy resolution for 1GeV photons as a function of the thickness of the scintillator. The triangles, black squares, and white squares show the resolution for 3 mm, 2 mm, and 1 mm thick lead, respectively. 16
2.4 The position resolution is shown as a function of the number of layers, n. In the upper graph, the position resolution becomes minimum at n=20, we decided to use the first 20 layers as the 1st block. Similarly, we studied the position resolution in the 2nd block by varying the number of layers, and decided to use from the 21th layer to 30th layer as the 2nd block in the middle figure. We decided to use the rest of the layers (from the 31th layer to 100th layer) as the 3rd block in the bottom figure. In this way, we divided the 100 layers into 3 blocks. 17
2.5 The fibers labeled "1" only read out the energy deposited in the area around the fiber in the 1st block. Similarly, the fibers labeled "2" and "3" only read out the square areas in block 2 and 3, respectively. 18
2.6 A setup for the light output measurement. The cell labeled 100 shows the position of a fiber which reads out the deposit energy. The numbers in cells show the normalized light output of the fiber when a laser light hits the cell. 19

3.1 A side of view of SHASHLIK 21
3.2 A photograph of lead/scintillator plate and the structure of the shashlik. 22
3.3 The concept of the method which the scintillation light is read out by the WLS fiber 22
3.4 The jig for align the fibers with the anodes of PMT. 24
3.5 The way of checking the cross-talk 24
3.6 A picture of the circuit board to read out multi anode PMT . . . 25
3.7 The setup to test the fiber blckout method 26

3.8 The ADC plot of the fiber blckout. The top figure is for normal fiber, the middle figure is for the fiber painted by a black magic marker, and the bottom figure is for the fiber painted by a black paint. We can reduce about 88% of the photon yield by black magic marker, about 95% of the photon by black paint, ... 26

4.1 A brief sketch of tagging counter 28
4.2 A brief sketch of tagging counter 30
4.3 A sketch of our detector setup for the shower profile measurement 31
4.4 This figure shows the setup for an angle measurement. The orange circles are beam incident positions, x=3.5 cm, 4.5 cm, and 5.5 cm, respectively. 31
4.5 Photograph of our detector setup. The leftmost detector covered with black sheet is a collimator. The detector next to the collimator is a charged veto counter. The rightmost detector is shashlik calorimeter. In this photograph, the photon beam comes from the left side. 32

5.1 The TDC distribution of the tagging counter. We required an in-time hit to have 600 counts $<$ TDC $<$ 800 counts for each tagging counter. 34
5.2 A sketch of the gain calibration for shower profile counter. And this shows also gain factor. 35
5.3 This shows the shower profile of Data and MC at different depths. Here we normalized the deposit energy of each fiber by requiring that the sum of energies of all 8 fibers is 1.0, where 8 fibers are located just above the beam hight. Black circles show the Data and the white circles show MC. 36
5.4 This shows the ratio of the MC to the Data, where the ratio is defined in Figure 5.3. The horizontal axis shows the radiation length and the vertical axis shows the ratio of MC to DATA for each fiber. CH means the position of a fiber. CHi is located at x=$i$cm. 37
5.5 This shows the shower development as a function of the depth for 10 different γ energis. A horizontal axis shows the radiation length and a vertical axis shows the relative sum of the deposit energies of 8 fibers (normalized at 5 X_0). White circles show MC and black circles show DATA. 38
5.6 A sketch of gain calibration for 'long counter'. we used Geant to inject photons at a certain x, and generated showers in the long counter. We then compared the output of 8 fibers at the same x between data and Geant, and used their ratio as a relative gain. This process was repeated from x=1cm to x=16cm. 39
5.7 This shows the gain factors of 'long counter' with 64 ch MAPMT. 39

6.1 This shows the correlation between the center of energy and the beam incident position. The horizontal axis shows the center of energy and the vertical axis shows the beam incident position. The top, middle, and bottom show the 1st, 2nd, 3rd block in depth, respectively. The curve shows the fitting function we used. 41
6.2 Position resolution is shown as a function of the beam incident position. The '8.5cm' corresponds to the border between two SHASHLIK with 64ch MAPMT. 42
6.3 The position resolution at the center of 3×3 shashlik is shown as a function of the photon energy for 0 and 5 degree incident angle. The top, and bottom show 0, and 5 degree incident angle, respectively. 42
6.4 This graphs show the correlation between incident angle and the transverse distance of the reconstructed positions between blocks. The left plots show the distances for block 3 -1, and the right plots show the distances for block 3 - 2. The incident photon positions are x=3.5 cm (top), 4.5 cm (middle), 5.5 cm (bottom). 44
6.5 The top shows the correlation between the reconstructed angle and incident angle. We see that there are some differences between them, and so we fitted the reconstructed angle vs. the incident angle for linear function. The bottom shows the differences between the reconstructed angle and the incident angle. . . 45
6.6 The graphs show the reconstructed angular distributions for 0, 5, 10, 15, and 20 degree incident angle as indicated in each plot. We defined the sigma of the fitted gaussian as the angular resolution. 45
6.7 This plot shows the dependence of the angular resolution as function of the beam energy for 0,5, 10, 15, and 20 degree incident angle as indicated in each plot. The curve shows the , $\frac{p1}{\sqrt{E}}$, where E is the incident photon energy. 46
6.8 This shows the typical ADC distribution for 4 different energy at x=4.5 cm. 47
6.9 The energy resolution as a function of energy at x=4.5 cm. The curve shows the fit function, $\sqrt{\frac{p1*p1}{E} + p2*p2}$, where E is the incident photon energy. 48

7.1 The dots shows the shower development shape of the data. Here the data is averaged of 8 different energies 50
7.2 This show the ratio between the two gain factor. 51
7.3 The energy dependence of the angular resolution for 0,5, 10, 15, and 20 degree incident angles after using the measured shower shape for calibration. Our fit function is $\frac{p1}{\sqrt{E}}$, where E is the incident photon energy. 52

8.1 The energy dependence of the angular resolution for 0,5, 10, 15, and 20 degree incident angles. Our fit function is $\frac{p1}{\sqrt{E}}$, where E is the incident photon energy. 55

List of Tables

3.1 Genaral parameter of the H7546B MAPMT 23

4.1 The table of the photon energy for each tagging counter 29
4.2 The summary of the detector 29

6.1 Fitting parameter for position reconstruction 40

Chapter 1

Introduction

The existence of symmetry principles in physics had been speculated as a manifestation of underlying beauty of the universe. From Newtonian mechanics to quantum mechanics, symmetry principles, connected with conservation laws, have provided us economical but elegant ways of looking at the nature. The law of right-left symmetry, associated with parity conservation, and invariance in charge conjugation operation, the two discrete symmetry laws which gained importance in quantum mechanics, had also been assumed to hold in subatomic world of physics. In this context, the breakdown of the combination of charge and parity symmetry in kaon decay, following parity violation discovered in weak interactions, had given us great impact on our view of the nature, At the same time, the discovery opened our eyes toward a new framework of physics. It helped us to establish a model of CP violation.

After about three decades since the CP breaking observation, so called the Standard Model has become believed to be the most probable candidate for the full description of elementary particle physics. Recent research had been focused the determination of the parameter of this scheme. In this respect, the kaon decay $K_L \to \pi^0 \nu\bar{\nu}$, has gained a key role for the determination of the parameters. We will describe the underlying physics, the purpose and overview of this study in this chapter.

1.1 CP violation

The combination of charge conjugation and parity transformation changes K^0 into $\bar{K^0}$, and vice versa:

$$CP|K^0 >= |\bar{K^0} > . \tag{1.1}$$

$$CP|\bar{K^0} >= |K^0 > . \tag{1.2}$$

(We use a conventional phase definition, and currently neglect the small effect of CP violation.)

The eigenvalues and eigenstates of CP are described as:

$$K_1 = \frac{1}{\sqrt{2}}[|K^0> + |\bar{K^0}>](CP = +1) \tag{1.3}$$

$$K_2 = \frac{1}{\sqrt{2}}[|K^0> - |\bar{K^0}>](CP = -1) \tag{1.4}$$

K_2 is the longer-lived kaons, whose lifetime is 5.2×10^{-8} seconds, and K_1 is the short-lived kaons, whose lifetime is 0.89×10^{-10} seconds. It had been believed from CP consistency that K_2 decays to the three pions, which from a CP odd state, while K_1 decays to two pions in a CP even state.

In 1964, Cronin and Fitch, et al., observed that the longer-lived kaons decayed to two pions[1]. This suggests that CP odd long-lived kaons, K_L, decays into CP even mode, and CP is not conserved in this decay.

This phenomenon can be explained if K_L is actually composed not only of K_2 but also with a slight mixture of K_1:

$$K_L = \frac{1}{\sqrt{1+\epsilon^2}}[|K_2> + \epsilon|K_1>](CP = -1) \tag{1.5}$$

and K_1 decays to two pions. Such a mechanism for causing K_L to decay to two pions is called indirect CP violation. However, CP can be violated if K_2 in equation (1.5) decays to two π^0's. If K_2 directly decays to two pions, we can say that the CP is directly violated.

1.2 CKM matrix

The powerful framework to explain CP violation is the standard Model, which incorporates electromagnetic, weak, and strong interactions into a single scheme. It has a mechanism to introduce CP violation, including the direct CP violation.

In the Standard Model picture, direct CP violation is connected to the framework of quark mixing presented by Cabbibo, Kobayashi, and Maskawa. In this theory, direct CP violation stems from the consequence of a three generation model.

The charged current in weak interaction can be written as:

$$J^\mu = (\,\bar{u} \quad \bar{c} \quad \bar{t}\,)\,\frac{\gamma^\mu(1-\gamma^5)}{2} U \begin{pmatrix} d \\ s \\ b \end{pmatrix} \tag{1.6}$$

The matrix U, introduced by Kobayashi and Maskawa[2], tell us the coupling of up and down type quarks:

$$U = \begin{pmatrix} V_{ud} & V_{us} & V_{ub} \\ V_{cd} & V_{cs} & V_{cb} \\ V_{td} & V_{ts} & V_{tb} \end{pmatrix} \tag{1.7}$$

The 3 × 3 unitary matrix U can be represented by 4 parameters, with 5 arbitrary phase left aside. Of 4 parameters, 3 are real parameters and 1 is a complex phase factor which accounts for the CP violation.

Wolfenstein parameterized the matrix components as follows[3]:

$$U = \begin{pmatrix} \frac{1-\lambda^2}{2} & \lambda & A\lambda^3(\rho - i\eta) \\ -\lambda & \frac{1-\lambda^2}{2} & A\lambda^2 \\ A\lambda^3(1-\rho-i\eta) & -A\lambda^2 & 1 \end{pmatrix} \tag{1.8}$$

The η parameter accounts for the CP violation, and the determination of the η parameter is one of the primary goals of particle physics of today. As we will see, measurement of the branching ratio of rare CP violating decays can determine the value of η.

1.3 Decay of $K_L \to \pi^0\nu\bar{\nu}$

The observation of a rare decay $K_L \to \pi^0\nu\bar{\nu}$ is a good window to determine the η parameter. As shown in Figure 1.1, this decay is governed by short-distance transition current and occurs almost entirely from the direct CP violation, as described below.

The amplitude for $K_L \to \pi^0\nu\bar{\nu}$ can be written as

$$A(K_L \to \pi^0\nu\bar{\nu}) = \frac{1}{\sqrt{1+\epsilon^2}}[A(K_2 \to \pi^0\nu\bar{\nu}) + \epsilon(K_1 \to \pi^0\nu\bar{\nu})] \tag{1.9}$$

or

$$A(K_L \to \pi^0\nu\bar{\nu}) = \frac{1}{\sqrt{2(1+\epsilon^2)}}[(1+\epsilon)A(K^0 \to \pi^0\nu\bar{\nu}) - (1-\epsilon)(\bar{K^0} \to \pi^0\nu\bar{\nu})] \tag{1.10}$$

using equations (1.3) and (1.4). Since top quark can be in intermediate state (Figure 1.1), this decay involves to the V_{td} and V_{ts}. Using the Wollfenstein's parameterization (1.8),

$$A(K_L \to \pi^0\nu\bar{\nu}) \propto V_{td}^* V_{ts} - V_{ts}^* V_{td} \sim 2i\eta. \tag{1.11}$$

Thus, we can see the branching ratio of $K_L \to \pi^0\nu\bar{\nu}$ is proportional to η^2, and its measurement can determine the η parameter.

1.4 Background for $K_L \to \pi^0\nu\bar{\nu}$ experiment

There are several experiments to measure the branching ratio of $K_L \to \pi^0\nu\bar{\nu}$ decay. The theoretical estimate branching ratio is $\simeq 3.0\times10^{11}$. These experiments collect $K_L \to \pi^0\pi^0$ decays by detecting two photons originating from a

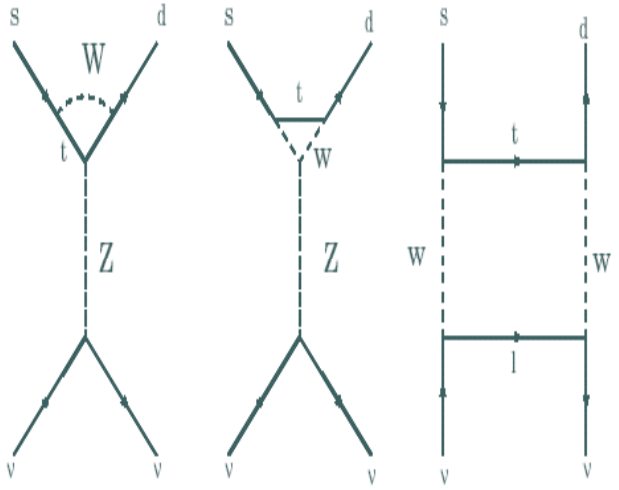

Figure 1.1: Feynman diagram for the decay $K_L \to \pi^0 \nu\bar{\nu}$

π^0 decay. This raises some difficulties for observing $K_L \to \pi^0 \nu\bar{\nu}$ due to background. Among various background sources such as $K_L \to \pi^0\pi^0$, $K_L \to \pi^0\pi^0\pi^0$, $K_L \to \gamma\gamma$, $K_L \to \pi^0\gamma\gamma$, etc, $K_L \to \pi^0\pi^0 \to \gamma\gamma\gamma\gamma$ decay with two missing photons is the main source of background. This is because its branching ratio is relatively high, $(9.14\pm0.34)\times10^{-4}$, and the decay has to miss only two photons. There are two categories of $K_L \to \pi^0\pi^0$ background; "Even pair" background, and "Odd" pair background. "Even pair" background events are caused by missing two photons originating from the same π^0s. "Odd pair" background events are caused by missing two photons originating from different π^0.

In the latter case, the reconstructed vertex, obtained by assuming that the two detected photons came from the same π^0, is different from the real vertex. Here the decay vertex can be calculated

$$m_{\gamma\gamma} = E_1 E_2 (1 - cos\theta) \tag{1.12}$$

where E_i are the energy of the photons, where θ is the angle between two photons, and by requiring that the vertex lies on the Kaon beam axis.

If we can measure the direction of the photon, we can suppress "odd pair"

background events whose photon directions do not point back to the reconstructed vertex. Thus the angle measurement will play an important role in $K_L \to \pi^0\nu\bar{\nu}$ experiment to reduce backgrounds.

1.5 Motivation and Overview

With the importance of angle measurement in mind, we developed a new type of photon detector which can measure the direction of the photon.

Detectors which can measure the direction of the photon have been already proposed by KOPIO group [4] and LHC group [5]. The detector by KOPIO group consists of multiple layers of an inactive converter material, dual coordinate drift chambers and scintillators. The chambers are used to track coverted electron position pairs and the scintillator counters are used for triggering, timing, and energy loss measurements. The angular resolution of this detector is 15 mrad at E_γ=450MeV. The detector by LHC group consists of a silicon strip preshower detector, followed by a lead scintillator sampling calorimeter which is read out by wave length shifting fibers. The angle is reconstructed by measuring the shower positions at the silicon strip, shower barycenter in the calorimeter. The measured angle resolution is $\frac{70mrad}{\sqrt{E}(GeV)}$.

Both detectors are expensive and have complex structures. Thus I wonder whether we can measure the angle by using a detector with a single structure. The concept of a new detector is that we separate the detector into two or three parts in the depth and measure the shower shape in each part. We can reconstruct the direction of the photon by fitting the positions at different depths. To keep the cost low, we will use a sandwich of lead and scintillator. The scintillation light is read out with wave length shifting fibers running perpendicular to the plates. The light output from fibers are measured individually to observe the shower shape.

We have designed, built, and tested such a direction sensitive calorimeter.

The next chapter will describe how we decided basic parameters of a new type of detector. Chapter 3 describes the details of this detector. Chapter 4 describes the overview of the experiment we ran at SPring8. Chapter 5 describes the gain correction of the detector. Chapter 6 will present the data analysis and Chapter 7 will present the systematic error. Chapter 8 describes Geant simulation. The discussion will be given in Chapter 9. At last, in Chapter 10, we will give the conclusion of this study.

Chapter 2

Study of basic parameters of a new photon detector

In this chapter, we will study and determine fundamental parameters of the detector.

2.1 The concept of a new detector

The essence of a new detector which can measure the direction of the photon is to measure the shower profiles at different depths. By fitting the transverse position of the shower center at different depths, we can reconstruct the angle as shown in Figure 2.1.

To design the detector, we also require two things. One is that the detector consists of only one module. The other is that we can handle it easily and construct it at a low cost.

Let us examine two types of detectors, Type1 and Type2, as shown in Figure 2.2. Two of them consist of lead and scintillator plates. They are generally called 'sandwich calorimeter' and are commonly used to measure the electromagnetic shower. Type1 reads out the scintillation light with fibers running parallel to the plates. Type2, which is generally called 'SHASHLIK', reads out the scintillation light with fibers running perpendicular to the plates. Comparing the two types, Type2 has an advantage that they can be stacked easily to construct larger detector. Thus we will study Type2 detector as a new photon detector in this thesis.

2.2 Geant Simulation

We will study basic parameters of a new shashlik type photon detector by using Geant simulation.

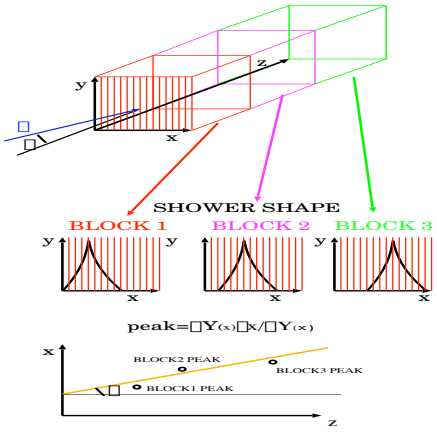

Figure 2.1: The strategy to measure the direction of the photon

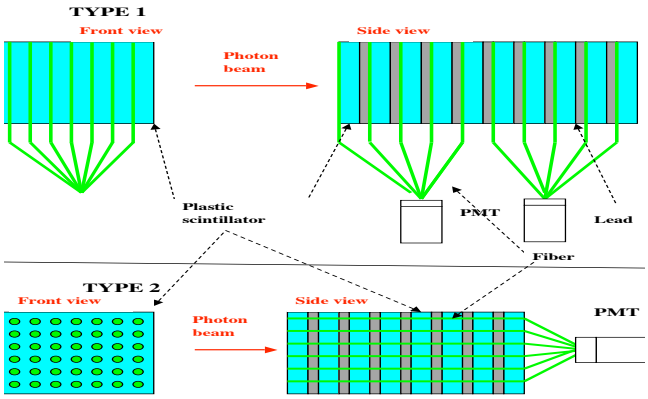

Figure 2.2: A design of a new photon detector

2.2.1 Thickness of lead and scintillator

First, we examine the best lead/scintillator combination. We varied the thickness of lead from 1 mm to 3 mm, and the thickness of scintillator from 1 mm to 5 mm. In the simulation, we assumed 100 layers of lead and scintillator plates each. The size of each plates was 24cm×24cm. Figure 2.3 shows the energy resolution for 1GeV photons for different thickness combinations. Based on this study, we decided the thicknesses of lead and scintillator to be 1 mm and 5 mm , respectively.

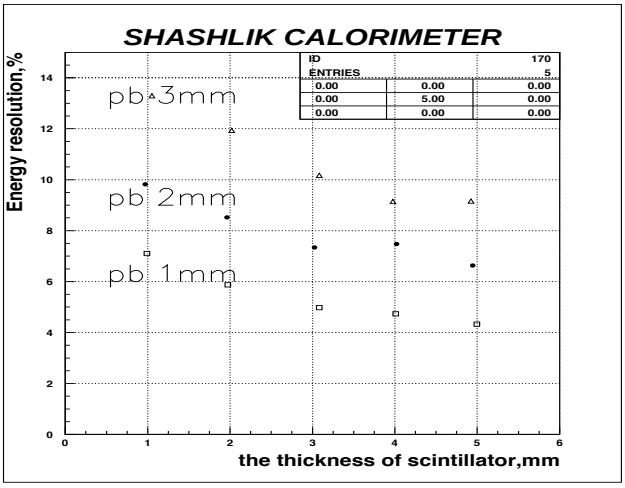

Figure 2.3: Energy resolution for 1GeV photons as a function of the thickness of the scintillator. The triangles, black squares, and white squares show the resolution for 3 mm, 2 mm, and 1 mm thick lead, respectively.

2.2.2 Optimum number of layers for each block

In order to measure the shower shape at different depths, we decided to divide the detector into three blocks in depth. We optimized the number of layers for each block in the following way. First, we divided each scintillator plate into 1cm wide strips (i=1....n), and injected photons into the same position of the detector. For the first n layers, we summed the deposit energy in the ith

strips along the depth and defined it as $E_{x(i)}$. The mean position is defined as $\Sigma(x(i)\times E_{x(i)})/\ \Sigma E_{x(i)}$, where $x(i)$ is the transverse position of the strip. The position resolution is defined by fitting the distribution of the mean position for Gaussian. Figure 2.4 shows the position resolution as a function of the number of layers, n.

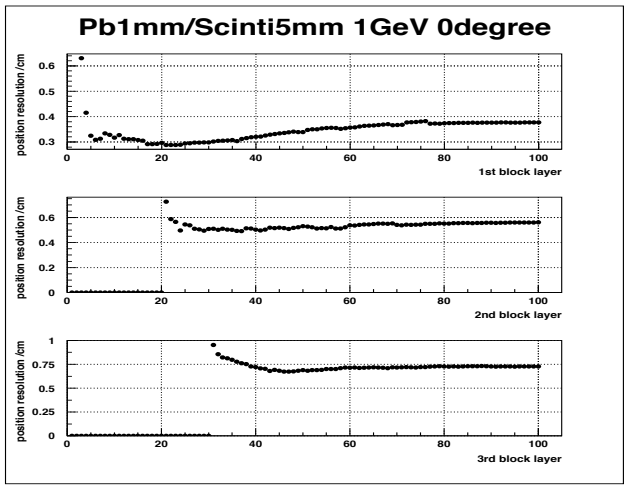

Figure 2.4: The position resolution is shown as a function of the number of layers, n. In the upper graph, the position resolution becomes minimum at n=20, we decided to use the first 20 layers as the 1st block. Similarly, we studied the position resolution in the 2nd block by varying the number of layers, and decided to use from the 21th layer to 30th layer as the 2nd block in the middle figure. We decided to use the rest of the layers (from the 31th layer to 100th layer) as the 3rd block in the bottom figure. In this way, we divided the 100 layers into 3 blocks.

Since the position resolution becomes minimum at n=20, we decided to use the first 20 layers as the 1st block. Similarly, we studied the position resolution in the 2nd block by varying the number of layers, and decided to use from the 21th layer to 30th layer as the 2nd block. We decided to use the rest of the layers (from the 31th layer to 100th layer) as the 3rd block. In this way, we divided the 100 layers into 3 blocks.

We plan to divide the detector into 3×3 modules whose size is 8cm×8cm. We read out the scintillation light from each module by 64 fibers going through

the scintillator plates. Each plate has 8×8 holes at 1cm interval. To measure the shower shape at three different depths, we decided that each fiber reads only one block, as shown in Figure 2.5. The fibers labeled "1" , "2", and "3" read out the energy deposited in the "1st", "2nd", and "3rd" block, respectively.

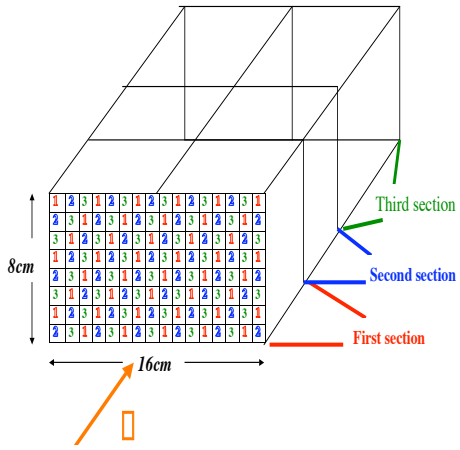

Figure 2.5: The fibers labeled "1" only read out the energy deposited in the area around the fiber in the 1st block. Similarly, the fibers labeled "2" and "3" only read out the square areas in block 2 and 3, respectively.

2.3 Fiber response test for GEANT simulation

In the previous section, we determined the basic parameters of the detector. In order to compare the simulation with experimental data in the later chapter, we need to evaluate the light output of each fiber as a function of the distance from the scintillation point.

Figure 2.6 shows the setup for this measurement. We guided the UV light pulse from a Nitrogen laser into the scintillator through a 0.5 mm quartz fiber to excite a localized spot in the scintillator. By moving the excited position, we read out one of 64 fibers on the scintillator.

In Figure 2.6, the cell labeled 100 shows the position of a fiber which read out the deposit energy. The numbers in cells show the light output of the fiber when a laser light hits the cell. The light output is normalized to the cell being read out, and shown in percentage. We divided the scintillator into two areas, middle area and outer area because the fiber responses were different. These responses were used to convert the deposit energy into light yield in each fiber, in the simulations used for later chapters.

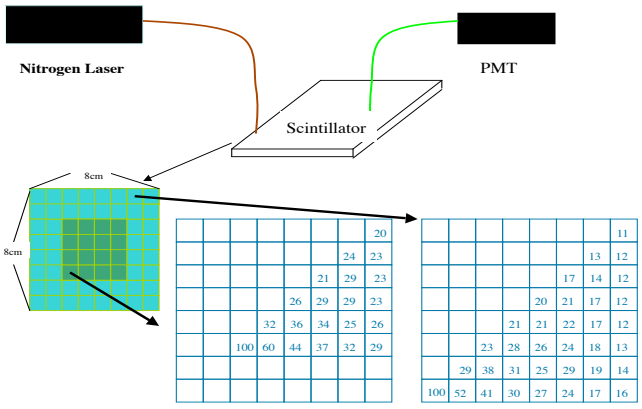

Figure 2.6: A setup for the light output measurement. The cell labeled 100 shows the position of a fiber which reads out the deposit energy. The numbers in cells show the normalized light output of the fiber when a laser light hits the cell.

Chapter 3

Shashlik calorimeter

In this Chapter, we described the element of the shashlik calorimeter that we built with the concept described in Chapter 2.

3.1 shashlik calorimeter

We made two kinds of calorimeters. One is a sandwich of 100 sheets of 1mm lead and 5mm scintillator plates with the total radiation length of 18 X_0. We will call this 'long counter'. We made 9 modules of this type. The other is a sandwich of 5 sheets of 1mm lead and 5mm scintillator and we call this type 'shower profile counter'. The size of lead and scintillator for both types is 8cm $\times$ 8cm. Figure 3.1 shows a photograph of our shashlik.

Seven of the long counters are viewed by 2 inch photo multiplier tubes (PMT, Hamamatsu H1161). Two of the long counters and a shower profile counter are viewed by 64ch multi anode photo multiplier tubes(MAPMT, Hamamatsu H7546B). Multi Anode PMT enabled us to read out 64 individual WLS fibers with one tube and it is far less expensive than reading out each fiber with a different PMT. The characteristics of MAPMT is described in section 3.1.3.

3.1.1 Lead/Scintillator

We developed a method to cast a scintillator with 64 1.5 mm diameter holes by using mold and scintillator pellets. This method can make complete scintillator plates without machining and polishing, and thus is suitable for mass-production. This scintillator has high transparency. The surface is a little uneven but that will not affect the light yield. The light yield was 11 % less than the scintillator made with normal method with the same pellets.

For the lead plates including antimony, we machined 64 holes with 1.7 mm diameter.

For assembling, 10 sheets of lead and scintillator were tightened together as a mini-module by 2.0mm$^{\phi}$, 5.0 cm long screws at two corners as shown in Figure

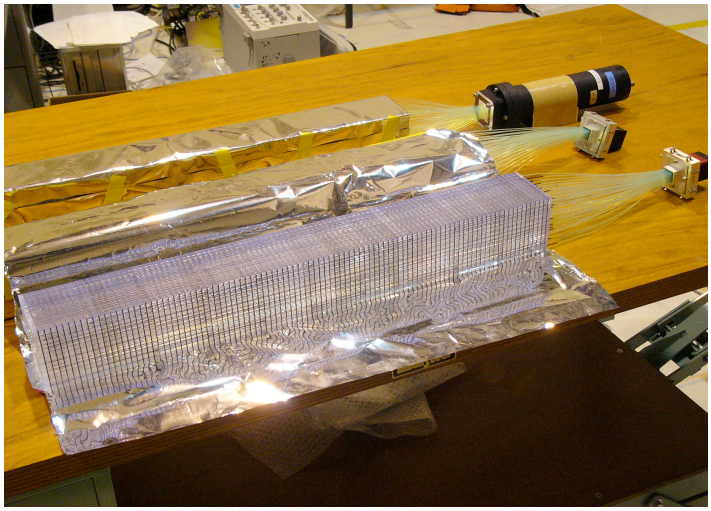

Figure 3.1: A side of view of SHASHLIK

3.2. The scintillator at the end of a mini-module was tightened with another 4 layers of lead/scintillators at the other two corners. By repeating this scheme, 100 layers were assembled into one module.

The construction of shashlik modules were manufactured by Hakuyo Engineering Co. (Higashiosaka-shi, Osaka).

.

3.1.2 Wave length shifting fiber

Principle

The concept of reading the scintillation light by WLS fibers is shown in Figure 3.3. When a charged particle goes through a scintillator, it emits light peaked at 420 mm. Some of the scintillation light are absorbed by the WLS fiber. The WLS fiber have a characteristic to emit light with longer wavelength (emission peak is about 450 nm). The light with the longer wavelength is transmitted through the WLS fiber to the PMT.

Requirements for the WLS fiber

The requirements for the WLS fiber are as follows:

1. The emission spectrum of the scintillator (emission peak is about 420 mm) overlaps with the absorption spectrum of the WLS fiber.

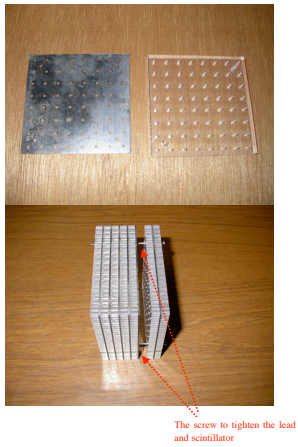

Figure 3.2: A photograph of lead/scintillator plate and the structure of the shashlik.

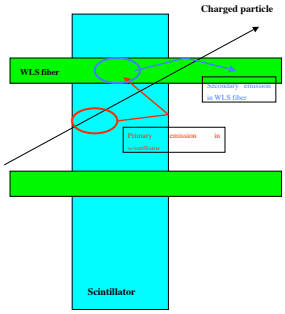

Figure 3.3: The concept of the method which the scintillation light is read out by the WLS fiber

2. The emission spectrum of the WLS fiber overlaps with the response wave length of 64ch PMT. (The wavelength of Maximum response is 420nm).

We selected Y11 from Kuraray as the suitable fiber for this experiment. There are two types of Y11; single cladding, and multi cladding. Multi cladding fiber has 50% higher light yield than single cladding fiber because of large light rapping efficiency. Thus we choose multi cladding Y11 fiber for this experiment.

3.1.3 64ch Multi Anode PMT

Characteristics

The table 3.1 shows the general characteristics of H7546B MAPMT.

Table 3.1: Genaral parameter of the H7546B MAPMT

Spectral Response	300 to 650 (nm)
Wavelength of Maximum Responce	420 (nm)
Photocathode	Bialkali
Dynode (number of stage)	12
Anode size	2×2 (mm^2)
Supply Voltage between anode and cathode	1000V (MAX)
Gain	3.0×2 (10^5)
Cross-talk (with 1mm Optical Fiber)	2%
Uniformity among all anodes	1:3

Alignment of the fibers with the anodes

We mounted the WLS fibers in a black plastic cube with 64 1.05 mm^{ϕ} holes by using optical cement as shown in Figure 3.4. The surfaces of the fibers were polished by a sand paper. We fitted the mount into a jig as shown in Figure 3.4. We use this jig to align the fibers with the PMT anodes.

Cross-talk

We aligned the fiber mount with MAPMT to minimize the cross-talk between the WLS fibers and the anodes. At first, we shined the blue LED light into a WLS fiber for the anode labeled 'A' shown in Figure 3.5. We define the ratio of the ADC output of the adjacent anode labeled 'B' to the labeled 'A' as cross-talk. In order to minimize this cross-talk, we made fine adjustments using screws on the jig. The final Cross-talk was less than about 3%.

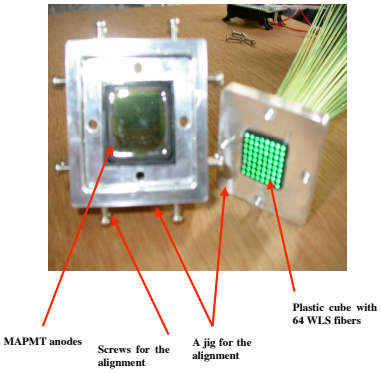

Figure 3.4: The jig for align the fibers with the anodes of PMT.

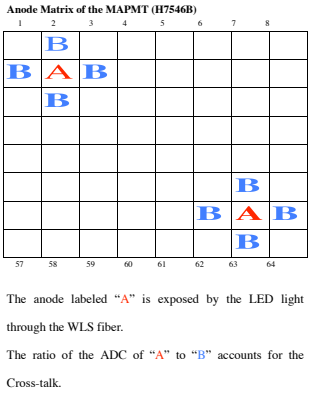

Figure 3.5: The way of checking the cross-talk

Read out system

We developed a circuit board for reading out the signals from the 64 ch MAPMT. This board is shown in Figure 3.6 has four 16 ch connectors and the signals are read out through coaxial cables.

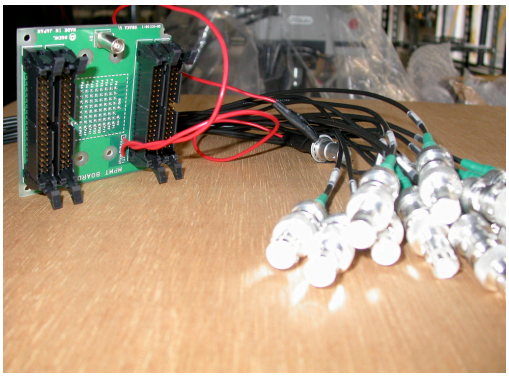

Figure 3.6: A picture of the circuit board to read out multi anode PMT

3.1.4 Fiber blackout

To measure the shower shape individually at different depths, we painted the WLS fibers in the regions where we do not read out the deposit energy. We prepared three types of fibers; normal fiber without paint, a fiber painted by a black magic marker, and a fiber painted by black paint. The setup for fiber black out measurement is shown in Figure 3.7. Each type of fiber is installed into a groove in a scintillator plate. We placed a Sr source at the center of scintillator, and measured the number of photons for each type of fiber. We define the ratio of the difference between ADC count and pedestal of painted fiber to normal fiber. Figure 3.8 shows the ADC counts for each type of fiber. We can reduce 88%, and 95% of the photon yield by Black magic marker, and black paint, respectively. Therefore we chose black paint to blind fibers.

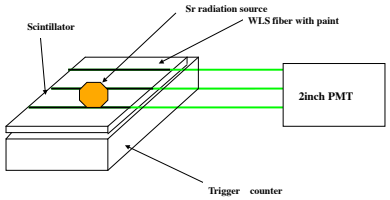

Figure 3.7: The setup to test the fiber blckout method

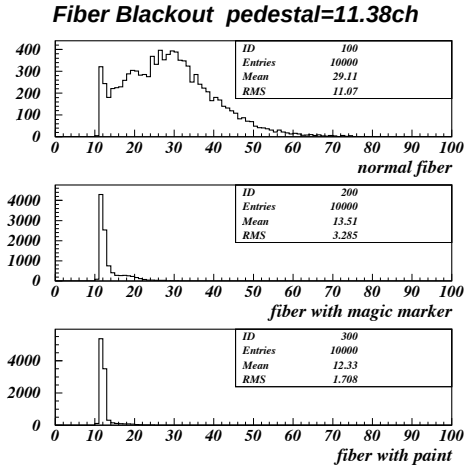

Figure 3.8: The ADC plot of the fiber blckout. The top figure is for normal fiber, the middle figure is for the fiber painted by a black magic marker, and the bottom figure is for the fiber painted by a black paint. We can reduce about 88% of the photon yield by black magic marker, about 95% of the photon by black paint,

Chapter 4

The outline of the experiment at SPring8

We tested our shashlik detector at SPring8. In this Chapter, we will describe the photon beam, the detector setup, the trigger and the data acquisition system.

4.1 Beam

We used the bremsstrahlung photons in the Laser Electron Photon beam line at SPring8. The momentum of the electron after the bremsstrahlung is measured by tagging counters which were placed at the inner side of the storage ring as shown in Figure 4.1. The tagging counters consist of 10 plastic scintillators. We numbered the tagging counter as tag$i$, as shown in Figure 4.2. The energy of the photon for each tagging counter is shown in Table 4.1[6]

4.2 Detector summary

In this section we describe the detectors used for the experiment. Table 4.2 shows their summary.

4.2.1 Collimater

In order to narrow the beam size, we put an active collimator 750 mm upstream of the front of the shashlik. The collimater has a 3.5 mm diameter hole, and consists of 17 sheets of 1.5 mm thick lead and 5mm thick plastic scintillator with the total radiation length of 4.63 X_0. The size was 15 cm $\times$ 15cm. The collimater is viewed by a 2 inch PMT.

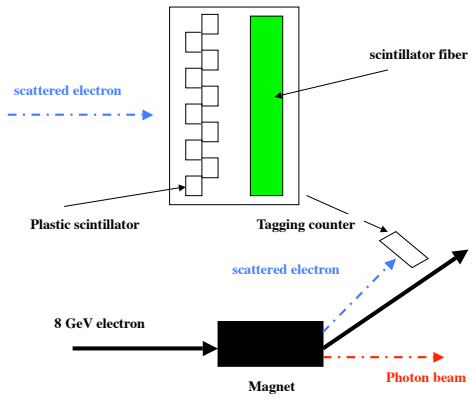

Figure 4.1: A brief sketch of tagging counter

4.2.2 Veto counter

In order to detect charged particles which enter the SHASHLIK CALORIMETER, we put a veto counter 50 mm downstream of the Collimater. This veto counter is made of plastic scintillator and the size was 10 cm $\times$ 10 cm $\times$ 1 cm .

4.3 Experiment

In the experiment, we stacked 'long counter' in 3×3 matrix as shown in Figure 4.4. At first, we define the coordinates and the incident angle for this experiment. We define the position of the leftmost fiber of the two shashlik with 64ch MAPMT as x=1cm and the rotation to the left toward the beam axis as the incident angle as shown in Figure 4.4.

We made the following two measurements at SPring8.

One is a shower profile measurement. In order to compare MC and Data for shower development and profile and also to calibrate the detector, we measured a shower profile at different depths. We measured it at 2 X_0, 3X_0,4X_0, 5X_0, 6X_0, 7X_0, 8X_0, 10X_0, and 12X_0 by adding a dummy lead/plastic block upstream the shower profile counter. This setup is shown in Figure 4.3.

Another one is angle measurement. We stacked 3×3 shashlik modules as shown in Figure 4.4. We injected photons at 5 different directions, 0, 5, 10, 15, and 20 degrees, at 3 different positions, x=3.5 cm, 4.5 cm, and 5.5 cm as shown in Figure 4.4.

Figure 4.5 shows setup of our detector.

Table 4.1: The table of the photon energy for each tagging counter

tagging counter No.	Photon Energy
counter 1	1.494 to 1.596 GeV
counter 2	1.494 to 1.727 GeV
counter 3	1.695 to 1.944 GeV
counter 4	1.822 to 2.062 GeV
counter 5	2.004 to 2.228 GeV
counter 6	2.146 to 2.359 GeV
counter 7	2.308 to 2.481 GeV
counter 8	2.433 to 2.618 GeV
counter 9	2.574 to 2.724 GeV
counter 10	2.682 to 2.840 GeV

Table 4.2: The summary of the detector

SHASHLIK CALORIMETER (for the angle measurement) The size of one module is 8cm × 8cm × 60cm. The total size is 24cm × 24cm × 60cm with 9 modules which corresponds with 19 X_0. 2 modules are viewed by 64ch MAPMT (H7546B). 7 modules are viewed by 2inch PMT (H1161).
SHASHLIK CALORIMETER (for the shower shape measurement) The size of this module is 8cm × 8cm × 60cm which corresponds with 19 X_0. This module is viewed by 64ch MAPMT (H7546B).
Collimater The collimater consists of 17sheets of 1.5 mm lead and 17 sheets of 5mm plastic scintillator with 15 cm × 15cm which corresponds to 4.63 X_0 and has a 35mm diameter hole. This is viewed by 2inch PMT (H1161).
Veto counter This veto counter is made of plastic scintillator and the size is 10 cm × 10 cm × 1 cm . This is viewed by 2inch PMT (H1161).

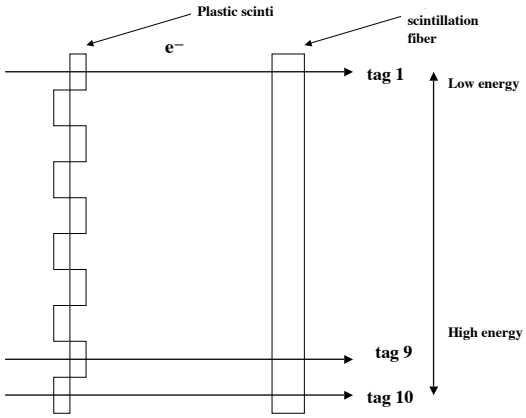

Figure 4.2: A brief sketch of tagging counter

4.4 Trigger

We used two types of triggers for this experiment. One is used for an angle measurement. This trigger required 50 MeV or more energy deposit in one of the two shashlik calorimeters with 64 ch MAPMT. Another trigger is used for the shower profile measurement. This trigger required 40 MeV or more energy deposit in the shower profile counter. The collimator and plastic scintillator were used to veto counters.

4.5 Data acquisition

Charges from PMT's were digitized by LeCroy FERA ADC, 2249W ADC, and the timing of the tagging counter were digitized by LeCroy 2228A TDC. The ADC's and TDC's were read out by TOYO CC/NET CRATE CONTROLLER, and the data were sent to PC via network.

In the experiment, the read out rate was 180 Hz and the dead time was 1.36 ms per event.

4.6 Run Summary

The data was taken from 20 November (2003) to 23 November (2003). We collected data for about 42 hours for angle measurements and 11 hours for the shower profile measurements.

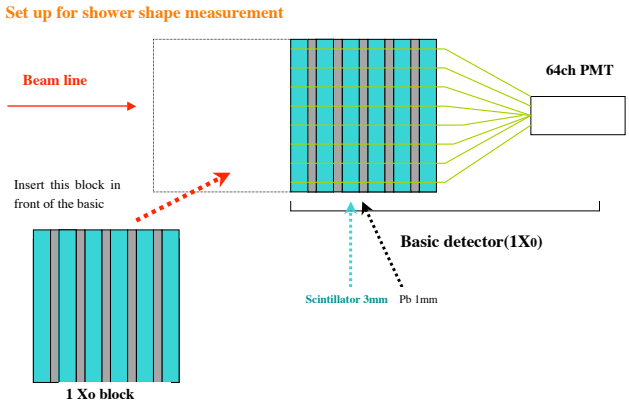

Figure 4.3: A sketch of our detector setup for the shower profile measurement

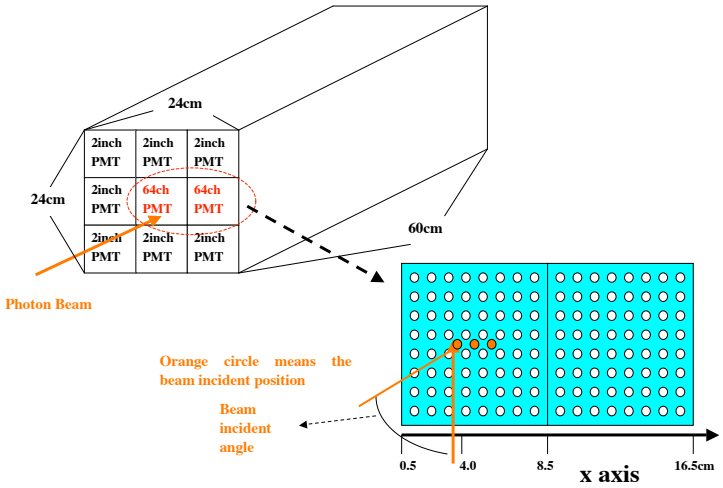

Figure 4.4: This figure shows the setup for an angle measurement. The orange circles are beam incident positions, x=3.5 cm, 4.5 cm, and 5.5 cm, respectively.

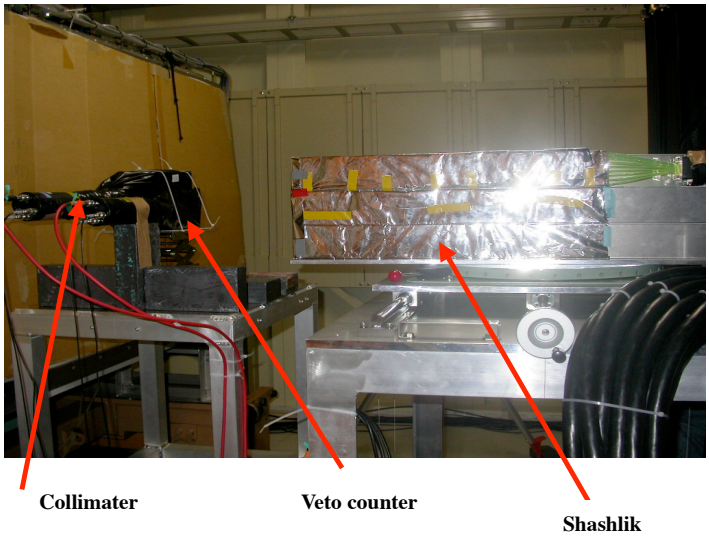

Figure 4.5: Photograph of our detector setup. The leftmost detector covered with black sheet is a collimator. The detector next to the collimator is a charged veto counter. The rightmost detector is shashlik calorimeter. In this photograph, the photon beam comes from the left side.

Chapter 5

Detector calibration

In this chapter, we will describe the event selection and detector calibration.

5.1 The flow of detector calibration

We first present the flow of the calibration.

1. Event selection
   We choose events where photon with known energy hit the detector.
2. Calibrate the gain of fibers in the shower profile counter
   By using the photon energy, we did gain calibration for the shower profile counter. We reconstruct the shower profile at the center of the detector by using that gain factor.
3. Compare the shower shape between data and MC.
4. Calibrate fibers in the long counters
   We did it by applying the shower shape we got at No2, 3 process.

5.2 Event selection

We required that there is only one in-time hit in the tagging counter for each event. Figure 5.1 shows the typical TDC distribution of a tagging counter. We required an in-time hit to have TDC counts between 600 and 800.

5.3 Gain calibration of fibers in the shower profile counter

We injected photons at 1 cm interval, in 8 different positions on the shower profile counter as shown by red circles in Figure 5.2. Assuming that the light

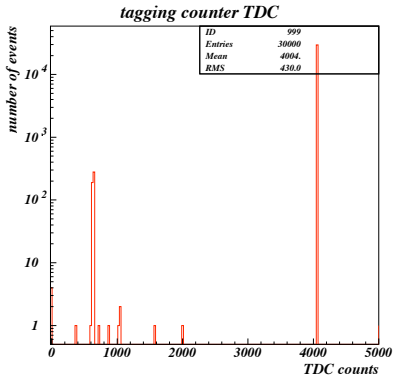

Figure 5.1: The TDC distribution of the tagging counter. We required an in-time hit to have 600 counts $<$ TDC $<$ 800 counts for each tagging counter.

output of the 4 fibers closest to the γ incident position were the same, we decided the relative gain of the 16 fibers near the beam height. The relative gain factors are also shown in Figure 5.2.

5.4 Comparison between shower profile counter and Geant Simulation

After correcting for the gain of the 16 fibers, we measured the shower shape for photons hitting at the center of the shower profile counter. We also simulated the shower profile by using Geant. Figure 5.3 shows the transverse shower profile obtained by 8 fibers just above the beam height for data and Geant at different depths. Here the sum of energies of in all 8 fibers is normalized to 1.0. There is a difference between data and Geant. Figure 5.4 shows the ratio of the MC to Data as function of radiation length at the beam height, where the ratio is defined in Figure 5.3. There is about 10 % difference between the MC and the Data, but we will neglect it for now. Figure 5.5 shows the shower development in all 8 fibers for data and Geant at different energies. We can see a difference between data and Geant at small radiation length. We evaluate it as the systematic error in Chapter 7.

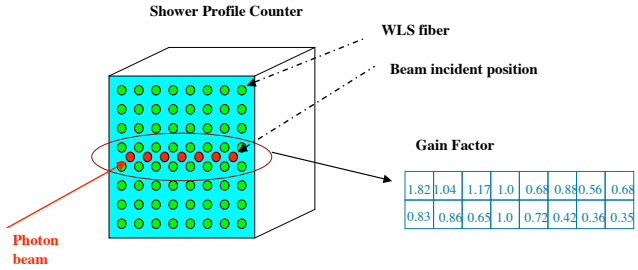

Figure 5.2: A sketch of the gain calibration for shower profile counter. And this shows also gain factor.

5.5 Gain calibration for SHASHLIK with 64ch MAPMT

In 'long counter' with 64 ch MAPMT, the adjacent fibers read out the deposit energy in different depth blocks as shown in Figure 2.5. Therefore, we cannot use the same calibration technique as for the profile counter. We calibrate the gain of each fiber in the long counter as follows. First, we used Geant to inject photons at a certain x, and generated showers in the long counter. We then compared the output of 8 fibers at the same x between data and Geant, and used their ratio as a relative gain. This process was repeated from x=1cm to x=16cm. A sketch of these process is shown in Figure 5.6. The gain factors are shown in Figure 5.7. We use these gain factors in the later chapter.

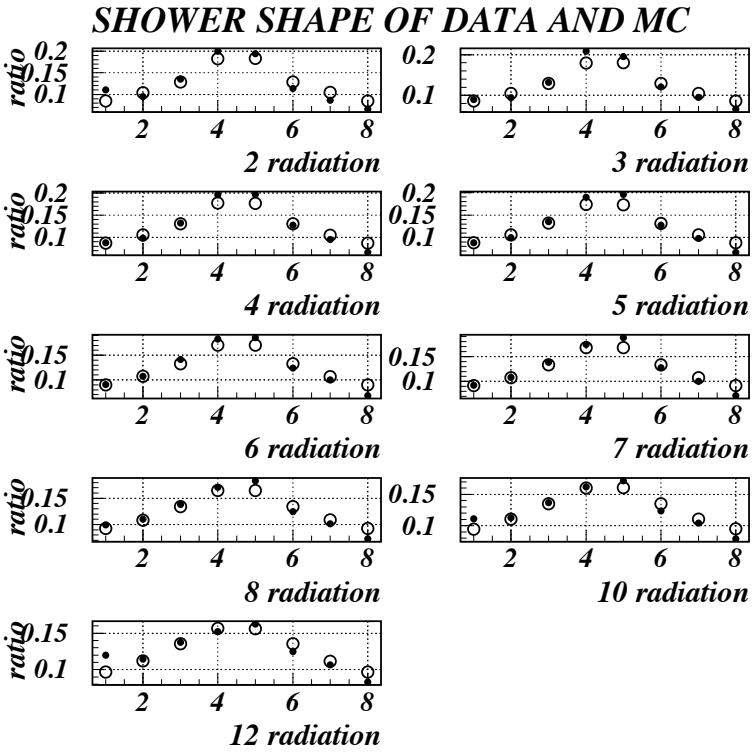

Figure 5.3: This shows the shower profile of Data and MC at different depths. Here we normalized the deposit energy of each fiber by requiring that the sum of energies of all 8 fibers is 1.0, where 8 fibers are located just above the beam hight. Black circles show the Data and the white circles show MC.

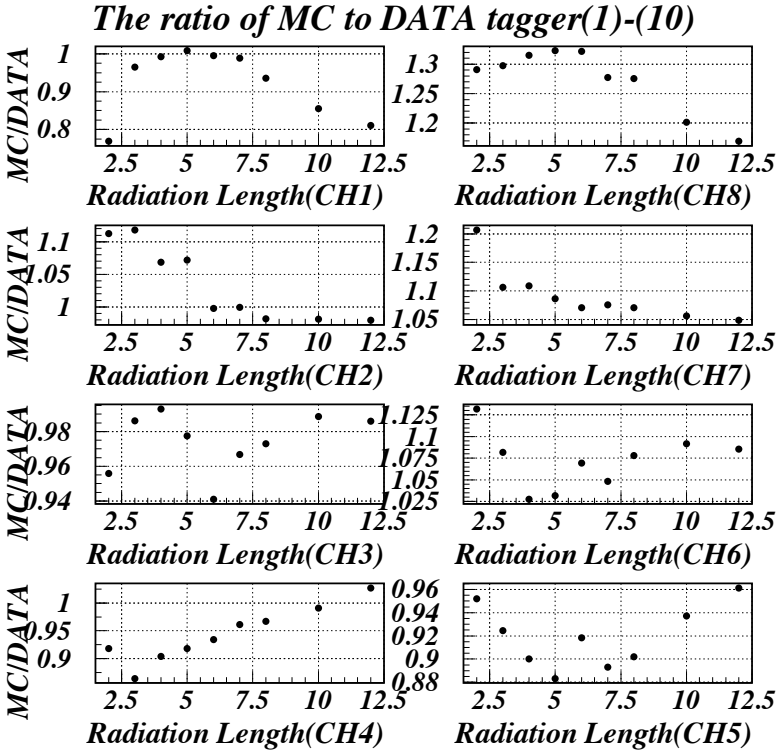

Figure 5.4: This shows the ratio of the MC to the Data, where the ratio is defined in Figure 5.3. The horizontal axis shows the radiation length and the vertical axis shows the ratio of MC to DATA for each fiber. CH means the position of a fiber. CHi is located at x=$i$cm.

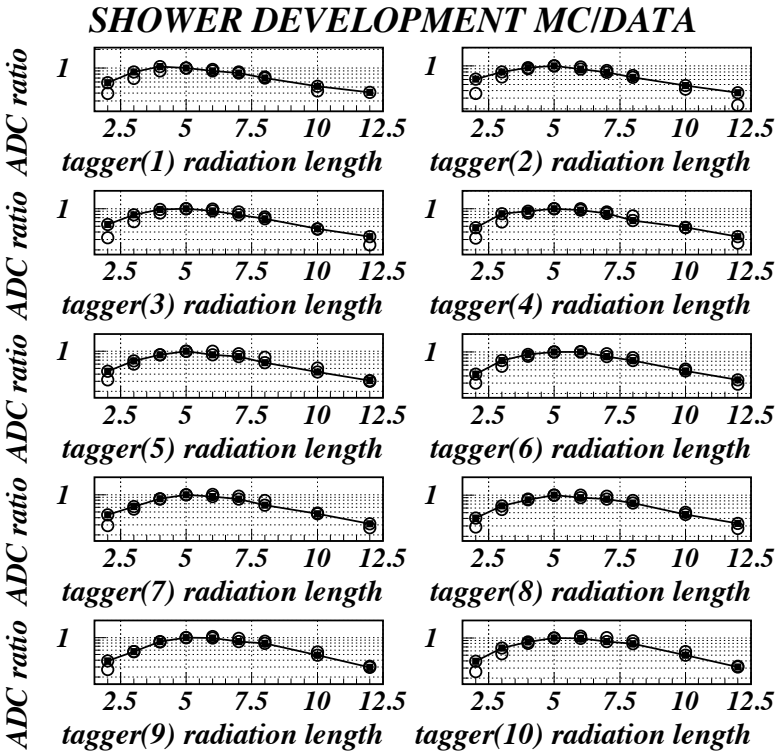

Figure 5.5: This shows the shower development as a function of the depth for 10 different γ energis. A horizontal axis shows the radiation length and a vertical axis shows the relative sum of the deposit energies of 8 fibers (normalized at 5 X_0). White circles show MC and black circles show DATA.

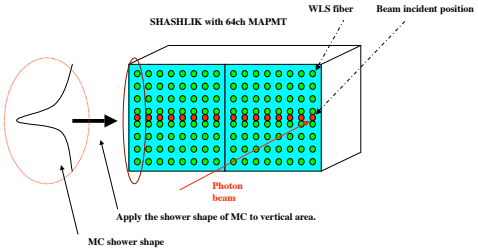

Figure 5.6: A sketch of gain calibration for 'long counter'. we used Geant to inject photons at a certain x, and generated showers in the long counter. We then compared the output of 8 fibers at the same x between data and Geant, and used their ratio as a relative gain. This process was repeated from x=1cm to x=16cm.

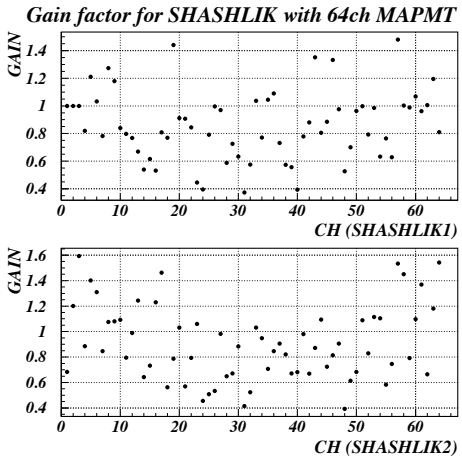

Figure 5.7: This shows the gain factors of 'long counter' with 64 ch MAPMT.

Chapter 6

Data Analysis

In this chapter, we will describe the position, angle, and energy resolutions.

6.1 Position resolution

First, we reconstruct the hit position of photons using the center of energy, $\Sigma(x(i)\times E_{x(i)})/\ \Sigma E_{x(i)}$, where $x(i)$ is the position of the fibers in x axis and $E_{x(i)}$ is the observed energy in the fiber. Figure 6.1 shows the beam incident position as a function of the the center of energy. We fit the correlation by a 4th order function,

$$p1 \times x^4 + p2 \times x^3 + p3 \times x^2 + p4 \times x + p5. \tag{6.1}$$

The fitted parameters for each block are shown in Table 6.1. We convert the center of energy to the reconstructed position by using this function.

Table 6.1: Fitting parameter for position reconstruction

Block No.	P1	P2	P3	P4	P5
Block 1	0.001463	0.01455	-1.036	10.59	-24.33
Block 2	0.001199	0.01702	-0.9849	10.23	-23.53
Block 3	0.001367	0.01497	-1.002	10.65	-25.61

Figure 6.2 shows the measured calorimeter position resolution. The resolution largely varies on the beam incident position.

Figure 6.3 shows the position resolution at the center of 3×3 shashlik as a function of the photon energy for 0 and 5 degree incident angle. The position resolution for normal incident is:

$$\sigma_x(cm) = \frac{0.45 \pm 0.08}{\sqrt{E}} + (0.57 \pm 0.06) \tag{6.2}$$

at the center of the 3×3 shashlik, where E is the photon energy in GeV.

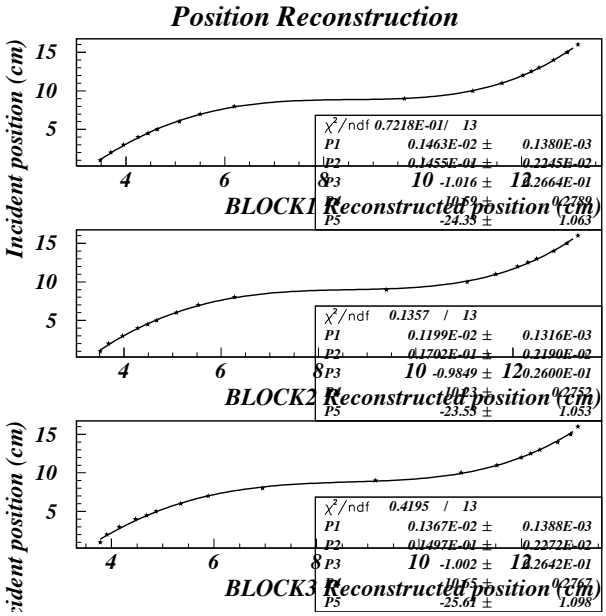

Figure 6.1: This shows the correlation between the center of energy and the beam incident position. The horizontal axis shows the center of energy and the vertical axis shows the beam incident position. The top, middle, and bottom show the 1st, 2nd, 3rd block in depth, respectively. The curve shows the fitting function we used.

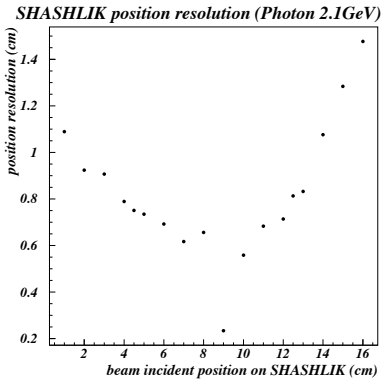

Figure 6.2: Position resolution is shown as a function of the beam incident position. The '8.5cm' corresponds to the border between two SHASHLIK with 64ch MAPMT.

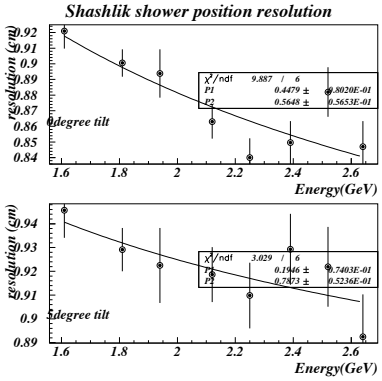

Figure 6.3: The position resolution at the center of 3×3 shashlik is shown as a function of the photon energy for 0 and 5 degree incident angle. The top, and bottom show 0, and 5 degree incident angle, respectively.

6.2 Angle resolution

The incident angle of photons is reconstructed in the following steps.

1. We reconstruct the shower center position in each block.
2. We reconstruct the angle by fitting the reconstructed positions at 3 depths.

For these steps, we need the effective depths of the three blocks. This will be described in section 6.2.1. The details of the angle reconstruction will be described in section 6.2.2.

6.2.1 Distances between the blocks

The effective depths of the three blocks is in the following steps.

1. We calculate the center of energy and reconstruct the transverse position in each Block.
2. We calculate the transverse distance between the reconstructed positions in block 1, block 2, and block 3 for 5 different incident angles, 0, 5, 10, 15, and 20 degrees.
3. We can get the effective distances in depth between the blocks from the correlation between transverse distance and the incident angles.

Figure 6.4 shows the correlation between the incident angles and the transverse distance of the shower center between blocks. The slope gives the effective longitudinal distance between blocks.

We averaged the slopes for three different incident positions, and decided the longitudinal distances between blocks as follows;

- block 1 to block 3 is 7.473 cm.
- block 1 to block 2 is 2.105 cm.
- block 2 to block 3 is 5.368 cm.

6.2.2 Angle reconstruction

We reconstructed the incident photon angle by using effective longitudinal distances determined above.

Figure 6.5 shows the correlation between the reconstructed angle and the incident angle. We see that there are some differences between them, so we fitted the reconstructed angle vs. the incident angle for a linear function. After this correction, we can determine the angle within 1.5 degree error as shown in Figure 6.5.

Figure 6.6 shows the reconstructed angle distributions for various incident angles. We defined the sigma of the fitted gaussian as the angular resolution.

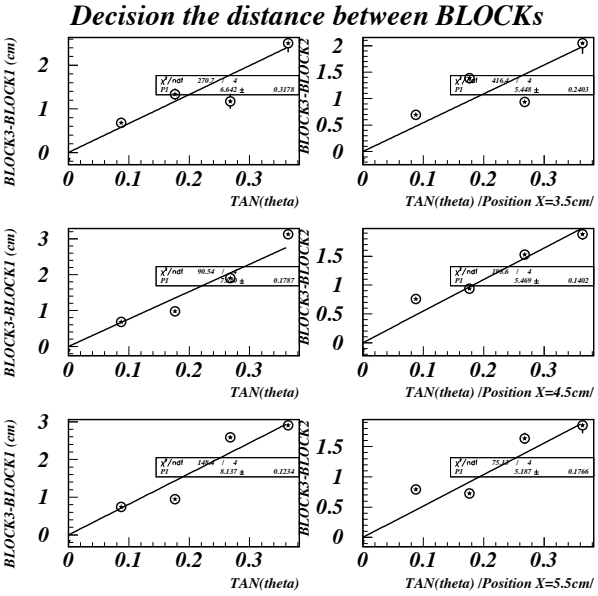

Figure 6.4: This graphs show the correlation between incident angle and the transverse distance of the reconstructed positions between blocks. The left plots show the distances for block 3 -1, and the right plots show the distances for block 3 - 2. The incident photon positions are x=3.5 cm (top), 4.5 cm (middle), 5.5 cm (bottom).

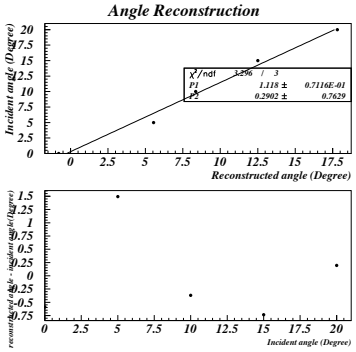

Figure 6.5: The top shows the correlation between the reconstructed angle and incident angle. We see that there are some differences between them, and so we fitted the reconstructed angle vs. the incident angle for linear function. The bottom shows the differences between the reconstructed angle and the incident angle.

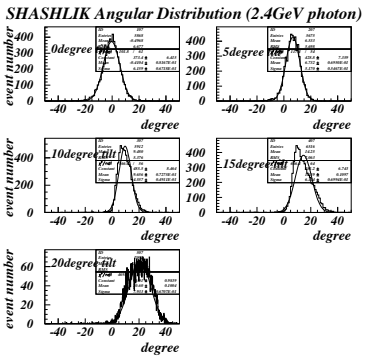

Figure 6.6: The graphs show the reconstructed angular distributions for 0, 5, 10, 15, and 20 degree incident angle as indicated in each plot. We defined the sigma of the fitted gaussian as the angular resolution.

Figure 6.7 shows the dependence of the angular resolution as function of the beam energy for incident angle. The fitted function is

$$\sigma_\theta = \frac{a}{\sqrt{E}} \tag{6.3}$$

where E is the photon energy in GeV, a is a coefficient.

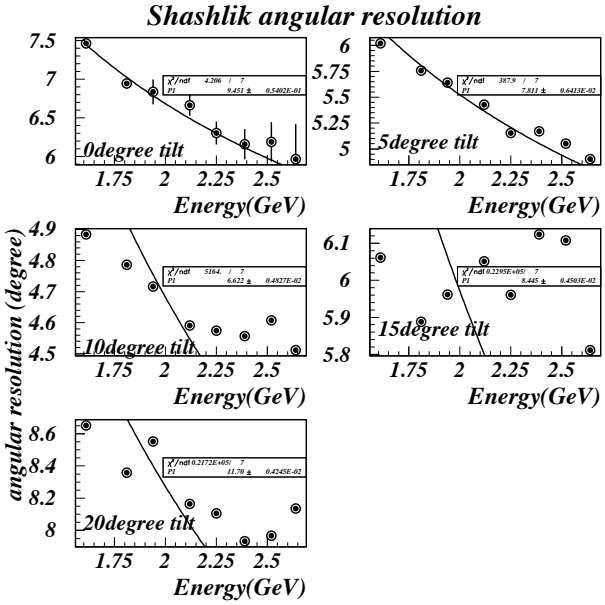

Figure 6.7: This plot shows the dependence of the angular resolution as function of the beam energy for 0,5, 10, 15, and 20 degree incident angle as indicated in each plot. The curve shows the ,$\frac{p1}{\sqrt{E}}$, where E is the incident photon energy.

We can get coefficient a for 5 different incident angles, 0, 5,10, 15, and 20 degree. Here we want to know the direction sensitivity of this detector, so we take the average of the coefficient a for each incident angle, $< a >$, as a representative angular resolution. As an error, we assigned the RMS of a. Thus we present the angular resolution as:

$$\sigma_\theta(degree) = \frac{8.80 \pm 1.71}{\sqrt{E}} \tag{6.4}$$

where E is the photon energy in GeV.

6.3 Energy resolution

Here we analyze the sum of energies of in shashlik modules with 64 ch MAPMT, which are the main modules for angle measurement. Figure 6.8 shows the typical ADC distribution for 4 different energies at x=4.5 cm. Here we define the sigma of the fitted gaussian as the energy resolution. Figure 6.9 shows the energy resolution as a function of the photon energy at x=4.5 cm. The energy resolution was found to follow:

$$\frac{\sigma_E}{E}(\%) = \frac{11.40 \pm 0.06}{\sqrt{E}} \oplus (0.0 \pm 0.7) \tag{6.5}$$

where E is the photon energy in GeV.

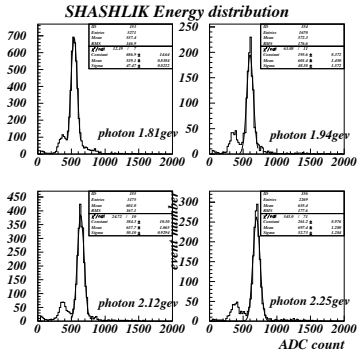

Figure 6.8: This shows the typical ADC distribution for 4 different energy at x=4.5 cm.

At last, we will describe the number of photo electrons. The charge of single photoelectron signal from 64 ch MAPMT was 0.36 pC. For 1.9GeV photon, the energy deposit in scintillator is 520 MeV, Therefore the photoelectron yield is 1.6 p.e./ MeV.

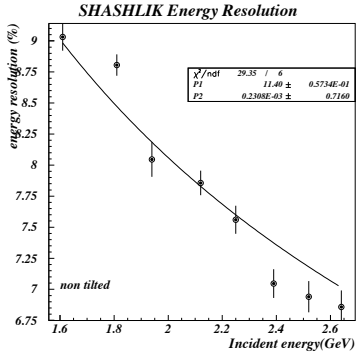

Figure 6.9: The energy resolution as a function of energy at x=4.5 cm. The curve shows the fit function, $\sqrt{\frac{p1*p1}{E} + p2*p2}$, where E is the incident photon energy.

Chapter 7

Systematic error on the angular resolution

In this chapter, we will discuss the systematic error.

There are two major sources for the systematic error on the angular resolution. One is the gain calibration we did in section 5.5. The other is the shower profile generated by Geant simulation in section 5.4.

7.1 Systematic error due to gain calibration

Here we evaluate the systematic error due to the gain calibration. When we calibrated the gain of each fiber in section 5.5, we used the mean energy for both MC and Data, but the mean value itself has an error. In order to study systematic error, we randomly varied the gains by gaussian with the error of the gains. We analyzed the data by using 5 different gain sets.

We obtained 5 different angular resolutions, R_i= $\frac{8.84}{\sqrt{E}}$, $\frac{8.82}{\sqrt{E}}$, $\frac{8.84}{\sqrt{E}}$, $\frac{8.78}{\sqrt{E}}$, and $\frac{8.84}{\sqrt{E}}$. We calculate the systematic error following as:

$$error = \sqrt{\frac{(R_i - R_m) * (R_i - R_m)}{5}} \tag{7.1}$$

where R_i is each resolution as described above, R_m=8.80 is the value we got in section 6.2. From this calculation the error is 0.03.

7.2 Systematic error due to the shower profile generated by Geant

We have been using shower shapes generated by Geant for calibration etc.. However, as shown in section 5.4, there is a difference in shower development

between data and MC. We will estimate the systematic error due to this difference by using the data shower shape. Figure 7.1 shows the shower development of the data. Here the data is the average of 8 different photon energies. We fit the shape for function:

$$Fitting function = 0.2523 * x^{2.166} * e^{-0.4323*x} \tag{7.2}$$

where x is the depth in radiation length.

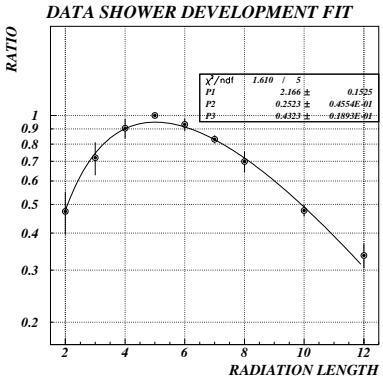

Figure 7.1: The dots shows the shower development shape of the data. Here the data is averaged of 8 different energies

We reevaluate the MC output value by using this function ((normalized at 5 X_0)). As we did in section 5.5, we decided the gain factor for shashlik with 64ch MAPMT by this MC output again. Figure 7.2 shows the ratio of the gain factor we got for systematic analysis to we got in section 5.5.

We reanalyzed the data by using these gain factors to see the effect.

Figure 7.3 shows the energy dependence of the angular resolution for 0, 5, 10,15, and 20 degree incident angles. The reanalyzed angle resolution is

$$\sigma_\theta = \frac{9.19 \pm 1.59}{\sqrt{E}} \tag{7.3}$$

We assign the differences (9.19-8.80=0.39) as this systematic error.

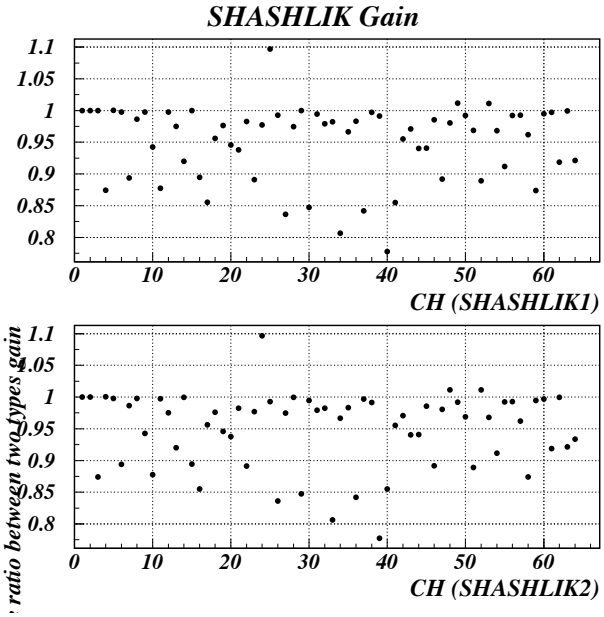

Figure 7.2: This show the ratio between the two gain factor.

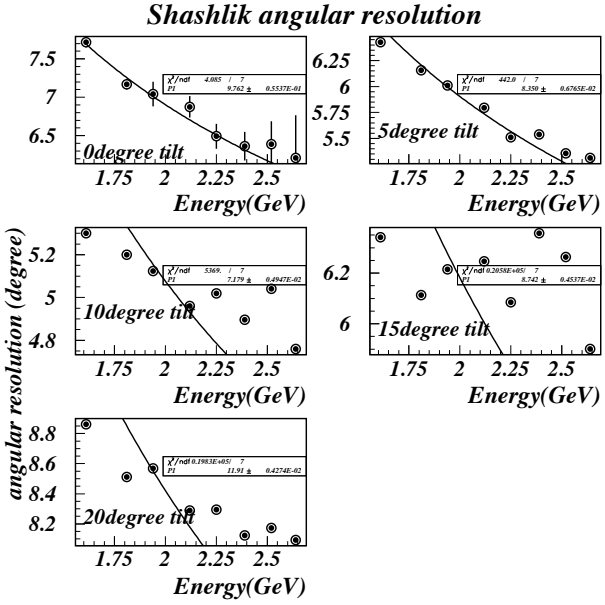

Figure 7.3: The energy dependence of the angular resolution for 0,5, 10, 15, and 20 degree incident angles after using the measured shower shape for calibration. Our fit function is $\frac{p1}{\sqrt{E}}$, where E is the incident photon energy.

7.3 Systematic error summary

By adding the two errors quadratically, we assign $\frac{0.39}{\sqrt{E}}$ degree as the systematic error for the angle resolution.

Chapter 8

Geant simulation

To understand the measured resolution, we ran Geant simulation. The beam size was 3.5 mm in diameter, which is the same with the photon beam size in the experiment. In the simulation, we took the number of photo electrons into account.

Angular resolution

Figure 8.1 shows the dependence of the angular resolution as function of the beam energy for 0, 5, 10, 15, and 20 degree incident angles.

Our fit function for systematic error:

$$\sigma_\theta(degree) = \frac{6.36 \pm 0.56}{\sqrt{E}} \tag{8.1}$$

where E is the photon energy in GeV.

Energy resolution

We analyzed the energy resolution. The function we fitted is

$$\frac{\sigma_E}{E}(\%) = \frac{7.41 \pm 0.02}{\sqrt{E}} \oplus (0.0 \pm 0.1) \tag{8.2}$$

where E is the photon energy in GeV.

Geant summary

We see a difference in the angular, and energy resolution between data and MC. We will discuss the reason in the next chapter.

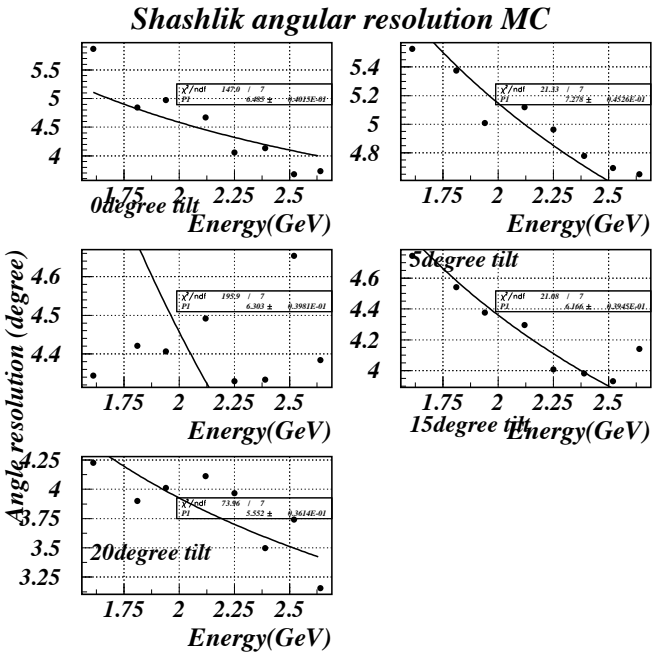

Figure 8.1: The energy dependence of the angular resolution for 0,5, 10, 15, and 20 degree incident angles. Our fit function is $\frac{p1}{\sqrt{E}}$, where E is the incident photon energy.

Chapter 9

Discussions

In this chapter, we discuss the improvements of the performance of the detector and analysis method.

9.1 The difference between the data and MC

Although the number of photoelectrons was taken into account, there is a difference between data and Geant as we have already seen is Chapter 6 and Chapter 8. There are two reasons. One is from the insufficient estimation of the fiber response as we did in section 2.3. We have done a rough calculation of evaluation for only 1cm×1 cm square area at that time, but we will have to test the response in a smaller step. The other is from the imperfect blackout for the fiber. In the current status, still 5% of the light leaks into fibers, and this affects the observes 'shower profile'. We will need to study more perfect shielding method.

9.2 Analytic method

We did the gain correction of the 64 ch MAPMT assuming that the shower profile of Geant was correct. For correcting the gain more precisely, we need to use the μ beam for the calibration. In this experiment, we took data at only 3 different incident positions, but we need to take more various position to discuss the angular resolution precisely. We also need more statistics to understand the detector better.

9.3 Improvements of the performances

The large resolution of angular, position, and energy will be from the lack of the photon yield. There are some methods to increase the number of photoelectrons as follows:

- We use a larger diameter fiber to catch more photons.

- We study better coupling between the surface of the fibers and the MAPMT anodes.
- We study the method to polish the fiber's face better than using the sand paper.
- To determine the position more precisely, we increase the density of the fibers.
- We need to study the best condition for molding, such as temperature or pressure because the light yield of the scintillator we used was 11 % less than the scintillator made by normal method.

Chapter 10

Conclusion

We studied a new photon detector which can measure the direction of the photon. For photons with the energies between 1.5 and 2.7 GeV, the angular resolution was $\frac{154\pm30_{(stat.)}\pm7_{(sys)}}{\sqrt{E}}$ (mrad), where E is the photon energy in GeV. At the center of the 3×3 shashlik tower, the position resolution was $(\frac{0.45\pm0.08}{\sqrt{E}} + (0.57 \pm 0.06))$ cm, and the energy resolution was $(\frac{11.40\pm0.06}{\sqrt{E}} \oplus (0.0 \pm 0.7))$ %, where E is the photon energy in GeV.

Bibliography

[1] J.Cronin, V.Fitch *et al.*, Phys.Rev.Lett. 13, 138(1964)

[2] M.Kobayashi and T.Maskawa, Prog. Theor. Phys. 49, 652(1973)

[3] L.Wolfenstein, Phys. Rev. Lett. 51, 1945(1983)

[4] I-H. Chinag *et al.*, "KOPIO -a search for $K_L \rightarrow \pi^0\nu\bar{\nu}$ MRE-Proposal, November 1(1999)

[5] P.Aspell *et al.*, "A Shashlik+Preshower Detector as Electromagnetic Calorimeter For LHC, CERN/DRDC94-97 RD36-Status Report, January 9(1995)

[6] A.Shimizu, Master Thesis, Osaka Univ., "The study of tagging counter using scintillation fibers at SPring-8/LEPS", (2004).